Nonspherical atomic effective pseudopotentials for surface passivation

Anastasia Karpulevich,[1,2] Hanh Bui,[1,2] Denis Antonov,[3] Peng Han,[1] and Gabriel Bester[1,2,*]
[1]*Institut für Physikalische Chemie, Universität Hamburg, Grindelallee 117, D-20146 Hamburg, Germany*
[2]*The Hamburg Centre for Ultrafast Imaging, Luruper Chaussee 149, D-22761 Hamburg, Germany*
[3]*Physikalisches Institut, Universität Stuttgart, Pfaffenwaldring 57, D-70569 Stuttgart, Germany*

(Received 1 July 2016; revised manuscript received 2 September 2016; published 14 November 2016)

We present a method to extract accurate pseudopotentials for surface passivants, within the framework of the atomic effective pseudopotential method. We retain the imaginary part of the pseudopotential in the construction procedure. This imaginary component in reciprocal space translates into a nonspherical component in real space. This asphericity allows to model surface dipoles and their ensuing band offsets. We show that these surface effects need to be taken into account to model electronic properties of quantum dots accurately—which requires to go beyond the spherical potential approximation for the passivant/surface atoms. The good level of transferability, without additional computational costs, is demonstrated for Si, CdSe, and InP nanostructures. The results are directly compared to large-scale density functional theory calculations.

DOI: 10.1103/PhysRevB.94.205417

I. INTRODUCTION

The quantum mechanical atomistic calculation of the electronic properties of colloidal semiconductor nanostructures, as they are encountered in experimental settings [1–5], is still challenging due to the large number of atoms involved. Structures with less than one thousand atoms are rarely investigated experimentally and this reciprocally represents the largest structures that can be treated by standard *ab initio* density functional theory (DFT). The atomic effective pseudopotentials (AEPs) [6,7], a further development of the empirical and semiempirical pseudopotentials [8–15,33], have been successfully used for large colloidal quantum dots (QDs) with up to 100 000 atoms [7,15]. However, the treatment of the surface remained at a quality well below a full fledged self-consistent *ab initio* treatment. Either the surface atoms were assumed to generate an electronic pseudopotential with a Gaussian shape determined by two or three parameters (depth, width and distance from the surface atom) that could be adjusted to free the optical gap of surface states [16,17], or the nanostructure was embedded in another artificial large band gap material [18–20]. A recent procedure [33] to extract passivant potentials based on DFT calculations and the semiempirical approach [8,9] used a spherical real-space description, required the adjustment of a passivant center (somewhat shifted with respect to the passivant position—already hinting at the nonspherical character of the passivant) and the fit to an *ad hoc* Yukawa potential. These procedures were justified, to a certain extent, for large nanocrystals (NCs) [21,22] or nanowires (NWs) [23], where the electronic states in proximity of the band gap region are well localized inside the nanostructure and only remotely affected by surface atoms. However, the influence of the surface on the electronic and optical properties is known to be significant. Moreover, the surface sensitivity represents one of the possible applications [1–5] of these nanostructures. Therefore an accurate quantitative treatment of surface effects is desirable.

In this work, we introduce a pseudopotential for surface or passivant atoms. We extract the passivant pseudopotential directly from *ab initio* DFT calculations without empirical parameters (in a procedure similar to the construction of bulk AEPs [6]). We thereby keep the imaginary part of the potential in reciprocal space, which corresponds to a real-space potential that has no inversion symmetry. This asphericity is shown to improve the quality of the results based on calculations of Si (group IV), InP (III-VI), and CdSe (II-VI) nanowires and Si quantum dots with more than thousand atoms. The results are directly compared to large-scale density functional theory results. A good level of transferability is thereby demonstrated with errors in the eigenvalues below 200 meV for challenging small structures, to below 50 meV for larger quantum dots. The nonspherical nature of the passivant AEP allows to reproduce the surface dipoles which generate a band offset to vacuum. The neglect of such effects is shown to lead to qualitatively erroneous results in Si NCs, especially for the unoccupied states. The new imaginary part allows us to simulate colloidal structures including the important surface contributions and comes at no additional computational cost, so that the AEP method can still address systems of one hundred thousand atoms [7]. A further positive feature of our approach is the fact that the passivant pseudopotentials are extracted from density functional theory by using a simple analytic connection between the Kohn-Sham potential and the atomic effective pseudopotential, which makes them parameter free and simple to derive.

II. METHODOLOGY

We solve a single-particle Schrödinger equation within a norm-conserving pseudopotential formalism [24,25]:

$$\left(-\frac{\hbar^2}{2m}\Delta + V^{\text{eff}}(\boldsymbol{r})\right)\psi_i(\boldsymbol{r}) = \varepsilon_i\psi_i(\boldsymbol{r}),$$
$$V^{\text{eff}}(\boldsymbol{r}) = V^{\text{ext}}(\boldsymbol{r}) + V^{\text{Hartree}}[n(\boldsymbol{r})] + V^{\text{xc}}[n(\boldsymbol{r})]. \quad (1)$$

The central quantity is thereby the effective Kohn-Sham potential V^{eff}. We use the frozen-core approximation [26] and norm-conserving pseudopotential in the Kleinman and

---

[*] gabriel.bester@uni-hamburg.de

Bylander separable form [27]. The effective self-consistent potential can be expressed as

$$\widehat{V}^{\text{eff}} = V^{\text{psp,loc}} + V^{\text{Hartree}}[n] + V^{\text{xc}}[n] + \sum_{lm} |\,\chi_{lm}^{\text{KB}}\rangle E_l^{\text{KB}} \langle\,\chi_{lm}^{\text{KB}}\,|, \qquad (2)$$

where the last term in Eq. (2) is the nonlocal part of the potential, E_l^{KB} are the Kleinman-Bylander eigenvalue and χ_{lm}^{KB} the normalized Kleinman-Bylander projectors. For details see also Ref. [6]. During the self-consistent cycle of the Kohn-Sham equations [Eq. (1)] the density is updated until the ground-state density n^{scf} is found. The starting point for the derivation of our AEPs is the local part of the self-consistent effective potential $V^{\text{eff}}(\boldsymbol{r})$:

$$V^{\text{loc}}(\boldsymbol{r}) = V^{\text{psp,loc}}(\boldsymbol{r}) + V^{\text{Hartree}}[n^{\text{scf}}] + V^{\text{xc}}[n^{\text{scf}}].$$

In this equation the $V^{\text{psp,loc}}$ are the norm-conserving pseudopotentials constructed using the approach of Troullier and Martins [28].

The potential belonging to a hermitian eigenvalue problem, such as our real-space local effective potential $V^{\text{loc}}(\boldsymbol{r})$, is real. Since we are using periodic boundary conditions, the potential is a periodic function and can be expanded in a Fourier series,

$$V^{\text{loc}}(\boldsymbol{r}) = \sum_{|\boldsymbol{G}|\leqslant G_{\max \text{V}}} V^{\text{loc}}(\boldsymbol{G})\text{e}^{i\boldsymbol{G}\boldsymbol{r}},$$

leading to the so-called $\boldsymbol{G}$-space potential,

$$V^{\text{loc}}(\boldsymbol{G}) = \frac{1}{\Omega_c}\int_{\Omega_c} V^{\text{loc}}(\boldsymbol{r})\text{e}^{-i\boldsymbol{G}\boldsymbol{r}}\,\text{d}^3\boldsymbol{r}, \qquad (3)$$

where Ω_c is the volume of the simulation cell. While the real-space potential $V^{\text{loc}}(\boldsymbol{r})$ is real but arbitrary in terms of its components, the $\boldsymbol{G}$-space potential obeys the symmetry $V^{\text{loc}}(\boldsymbol{G}) = V^{\text{loc}*}(-\boldsymbol{G})$; explicitly for the real and imaginary parts:

$$\begin{aligned}\text{Re}\,V^{\text{loc}}(\boldsymbol{G}) &= \text{Re}\,V^{\text{loc}}(-\boldsymbol{G}),\\ \text{Im}\,V^{\text{loc}}(\boldsymbol{G}) &= -\,\text{Im}\,V^{\text{loc}}(-\boldsymbol{G}),\end{aligned}$$

and, of course, does not carry more information than the real-space potential. From Eq.(3), it is easy to see that a real-space potential with inversion symmetry $V(\boldsymbol{r}) = V(-\boldsymbol{r})$ transforms into a real $\boldsymbol{G}$-space potential. A special case thereof being a spherically symmetric real-space potential $V(\boldsymbol{r}) = V(|\boldsymbol{r}|)$ leading to a vanishing imaginary part of the $\boldsymbol{G}$-space potential as well as a spherically symmetric $\boldsymbol{G}$-space potential $V(\boldsymbol{G}) = V(|\boldsymbol{G}|)$. Reciprocally, any deviation from an inversion symmetric real-space potential leads to a nonzero imaginary part in the $\boldsymbol{G}$-space potential.

In the AEP method [6], the total potential is defined as a sum of atom centered pseudopotentials:

$$V^{\text{loc}}(\boldsymbol{r}) = \sum_{\alpha}^{N_{\text{species}}}\sum_{n}^{N_\alpha} v_\alpha(\boldsymbol{r} - \boldsymbol{\tau}_{\alpha n}), \qquad (4)$$

with N_α atoms of type α. Each atom is centered at the position $\boldsymbol{\tau}_{\alpha n}$. The total $\boldsymbol{G}$-space potential is defined as

$$V^{\text{loc}}(\boldsymbol{G}) = \sum_{\alpha}^{N_{\text{species}}}\sum_{n}^{N_\alpha} \text{e}^{-i\boldsymbol{G}\cdot\boldsymbol{\tau}_{\alpha n}}\widetilde{v}_\alpha(\boldsymbol{G}) \quad \text{with}$$

$$\widetilde{v}_\alpha(\boldsymbol{G}) = \frac{1}{\Omega_c}\int_{\infty} v_\alpha(\boldsymbol{r})\text{e}^{-i\boldsymbol{G}\boldsymbol{r}}\,\text{d}^3\boldsymbol{r}, \qquad (5)$$

where we define $v_\alpha(\boldsymbol{G})$ without volume normalisation Ω_c, as

$$v_\alpha(\boldsymbol{G}) = \int_{\infty} v_\alpha(\boldsymbol{r})\text{e}^{-i\boldsymbol{G}\boldsymbol{r}}\,\text{d}^3\boldsymbol{r} = \Omega_c\widetilde{v}_\alpha(\boldsymbol{G}).$$

With this definition, Eq. (5) becomes

$$V^{\text{loc}}(\boldsymbol{G}) = \frac{1}{\Omega_c}\sum_{\alpha}^{N_{\text{species}}}\sum_{n}^{N_\alpha} \text{e}^{-i\boldsymbol{G}\cdot\boldsymbol{\tau}_{\alpha n}} v_\alpha(\boldsymbol{G}), \qquad (6)$$

where $v_\alpha(\boldsymbol{G})$ are the AEPs for the different atomic types. The AEPs have been defined as spherically symmetric in real space, which translates into a real $\boldsymbol{G}$-space potential $v_\alpha(\boldsymbol{G}) = v_\alpha(|\boldsymbol{G}|)$. The spherical approximation applied to bulk materials using AEPs [6,7], or traditional empirical pseudopotentials [10–14], or semiempirical pseudopotentials [8,9] leads to small errors in the eigenvalues resulting in a band gap error of around 60 meV according to Ref. [8], and more specifically of 87 meV for Si, 57 meV for InP, and 8 meV for CdSe according to Ref. [6]. Also within the *ab initio* DFT community, the muffin-tin approximation [29–31] relies on a spherically symmetric total effective potential.

Now we introduce the passivant by rewriting the potential from Eq. (6) explicitly for a binary cation-anion system with two types of passivants denoted by v_{H1} and v_{H2}:

$$\begin{aligned}\Omega_c V^{\text{loc}}(\boldsymbol{G}) = &\left(\sum_{n}^{N_{\text{cat}}} \text{e}^{-i\boldsymbol{G}\cdot\boldsymbol{\tau}_{\text{cat},n}}\right) v_{\text{cat}}(\boldsymbol{G})\\ &+\left(\sum_{n}^{N_{\text{ani}}} \text{e}^{-i\boldsymbol{G}\cdot\boldsymbol{\tau}_{\text{ani},n}}\right) v_{\text{ani}}(\boldsymbol{G})\\ &+\left(\sum_{n}^{N_{\text{H1}}} \text{e}^{-i\boldsymbol{G}\cdot\boldsymbol{\tau}_{H1,n}}\right) v_{\text{H1}}(\boldsymbol{G})\\ &+\left(\sum_{n}^{N_{\text{H2}}} \text{e}^{-i\boldsymbol{G}\cdot\boldsymbol{\tau}_{H2,n}}\right) v_{\text{H2}}(\boldsymbol{G})\\ = &\; S_c v_{\text{cat}}(\boldsymbol{G}) + S_a v_{\text{ani}}(\boldsymbol{G})\\ &+ S_{H1} v_{\text{H1}}(\boldsymbol{G}) + S_{H2} v_{\text{H2}}(\boldsymbol{G}),\end{aligned}$$

where $S_{c,a,H1,H2}$ are the structure factors of the cations, anions, and of the passivants $H1$ and $H2$ that are bound to the cations or anions, respectively. The structure factors depend only on the atomic positions. Reordering the terms, we obtain,

$$S_{H1} v_{\text{H1}}(\boldsymbol{G}) + S_{H2} v_{\text{H2}}(\boldsymbol{G}) = \Omega_c V^{\text{loc}}(\boldsymbol{G}) - S_c v_{\text{cat}}(\boldsymbol{G}) - S_a v_{\text{ani}}(\boldsymbol{G}),$$

where all is known but $v_{\text{H1,2}}(\boldsymbol{G})$, which we keep as complex quantities. To solve the equation of two unknowns we introduce a second system (in practice a second slab, see below) and denote both systems with A and B in

$$\begin{aligned} S^A_{H1} v_{\rm H1}(\boldsymbol{G}) + S^A_{H2} v_{\rm H2}(\boldsymbol{G}) &= \Omega_c V^{\rm loc}_A(\boldsymbol{G}) - S^A_c v_{\rm cat}(\boldsymbol{G}) \\ &\quad - S^A_a v_{\rm ani}(\boldsymbol{G}) \\ S^B_{H1} v_{\rm H1}(\boldsymbol{G}) + S^B_{H2} v_{\rm H2}(\boldsymbol{G}) &= \Omega_c V^{\rm loc}_B(\boldsymbol{G}) - S^B_c v_{\rm cat}(\boldsymbol{G}) \\ &\quad - S^B_a v_{\rm ani}(\boldsymbol{G}). \end{aligned}$$

We take the sum and difference of both equations and obtain the system of equations:

$$\boldsymbol{A}\boldsymbol{x} = \boldsymbol{B} \quad \text{with} \quad \boldsymbol{A} = \begin{pmatrix} S^A_{H1} + S^B_{H1} & S^A_{H2} + S^B_{H2} \\ S^A_{H1} - S^B_{H1} & S^A_{H2} - S^B_{H2} \end{pmatrix},$$

$$\boldsymbol{x} = \begin{pmatrix} v_{\rm H1}(\boldsymbol{G}) \\ v_{\rm H2}(\boldsymbol{G}) \end{pmatrix}, \tag{7}$$

$$\boldsymbol{B} = \begin{pmatrix} \Omega_c\big(V^{\rm loc}_A(\boldsymbol{G}) + V^{\rm loc}_B(\boldsymbol{G})\big) - \big(S^A_c + S^B_c\big)v_{\rm cat}(\boldsymbol{G}) - \big(S^A_a + S^B_a\big)v_{\rm ani}(\boldsymbol{G}) \\ \Omega_c\big(V^{\rm loc}_A(\boldsymbol{G}) - V^{\rm loc}_B(\boldsymbol{G})\big) - \big(S^A_c - S^B_c\big)v_{\rm cat}(\boldsymbol{G}) - \big(S^A_a - S^B_a\big)v_{\rm ani}(\boldsymbol{G}) \end{pmatrix}.$$

For the choice of the structures A and B used to derive the passivant AEPs, we look at three target properties. First, the supercell should be large in one dimension, in order to lead to a dense grid of $\boldsymbol{G}$-points along the extended supercell direction. Second, the system should not be too large, i.e., to still be manageable by standard DFT (from which we obtain the $V^{\rm loc}_{A,B}$). Third, the physical situation should be representative of the situation encountered in the "real" calculation, i.e., for the calculation of nanostructures (NWs, NCs, QDs). It turns out, that a slab geometry as shown in Fig. 1(a) is the most suitable. Both systems A and B differ only in the length of the slabs used, while the size of the supercell and hence the FFT grid of $\boldsymbol{G}$ vectors is kept constant. We use a small slab with 12 and one larger slab with 16 atoms [as depicted in Fig. 2(a)]. The atomic positions can be relaxed or not, which does not have an impact on the resulting passivant AEP; a feature that has to be fulfilled since transferability is a required property of the AEPs. From the full $\boldsymbol{G}$-space potential obtained from the self-consistent DFT calculations $V^{\rm loc}_{A,B}(\boldsymbol{G})$ we only use the grid points along the extended direction of the supercell (the slab [111] direction), which is the z-direction in our case:

$$V^{\rm loc}_{A,B}(\boldsymbol{G}) \equiv V^{\rm loc}_{A,B}(0,0,G). \tag{8}$$

The solution of Eq. (7) gives us $v_{\rm H1,2}(G)$, where G is the length of the considered $\boldsymbol{G}$ vector.

For the real component of $v_{\rm H1,2}(G)$, we make a spherical approximation: $\operatorname{Re} v_{\rm H1,2}(G) = \operatorname{Re} v_{\rm H1,2}(|G|)$. For

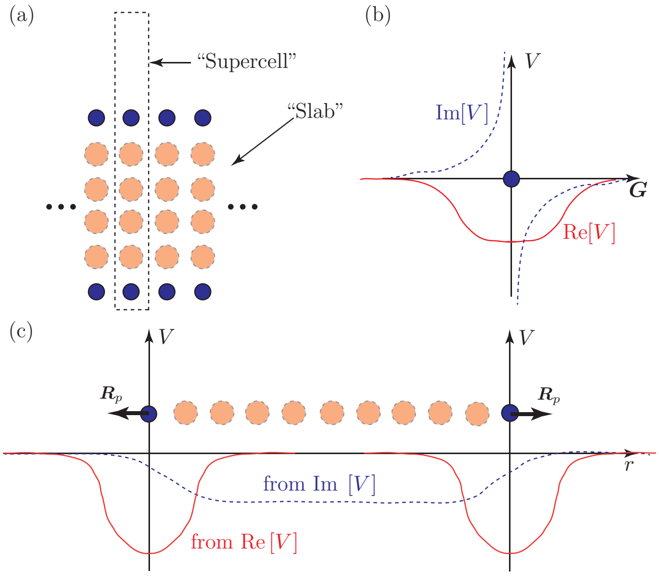

FIG. 1. (a) Schematic representation of the "slab" geometry used to calculate the passivant AEPs. (b) Real and imaginary components of the hydrogen (passivant) pseudopotential in reciprocal space. The imaginary part is odd and peaked towards $\boldsymbol{G} = 0$ with $\mathrm{Im}[V(\boldsymbol{G} = 0)] = 0$. (c) Potential in real space for two passivants with vectors pointing in opposite directions, corresponding to the situation in our slab geometries. The real-space potential (a real quantity) is divided into a part originating from the real $\boldsymbol{G}$-space potential and a part originating from the imaginary part of the $\boldsymbol{G}$-space potential.

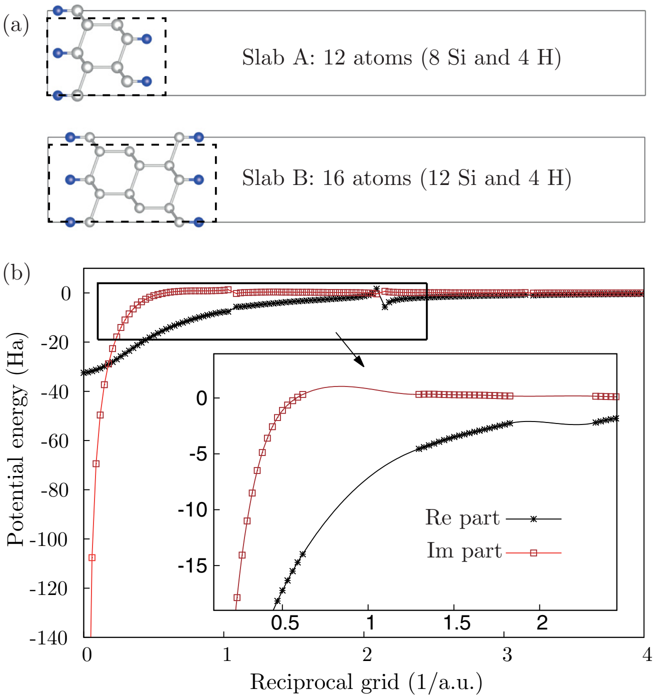

FIG. 2. (a) Atomic positions for silicon (gray) and hydrogen (blue) in slab A and slab B used in the extraction of the passivant AEPs. The slabs have zinc blende structure and the passivant atoms (blue) are pointing in the crystallographic [111] and $[\bar{1}\bar{1}\bar{1}]$ directions. (b) AEPs for the Si passivant as a function of $|\boldsymbol{G}|$, black stars represent the real part and red squares the imaginary part of the potential. The symbols (stars and squares) are the raw data points and the lines reproduce the final AEPs.

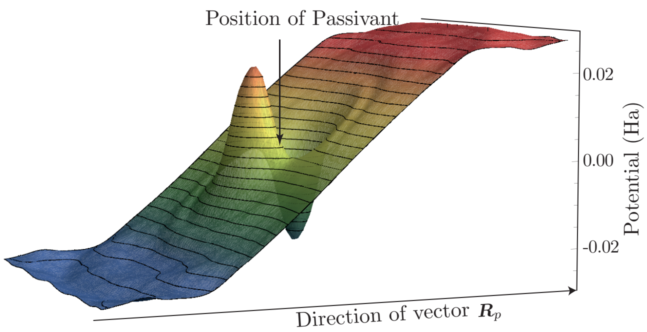

FIG. 3. Real-space potential of an isolated hydrogen passivant, when only the imaginary part of the $\boldsymbol{G}$-space AEP is considered. The passivant is oriented by the vector $\boldsymbol{R}_p$ [see Eq. (9)].

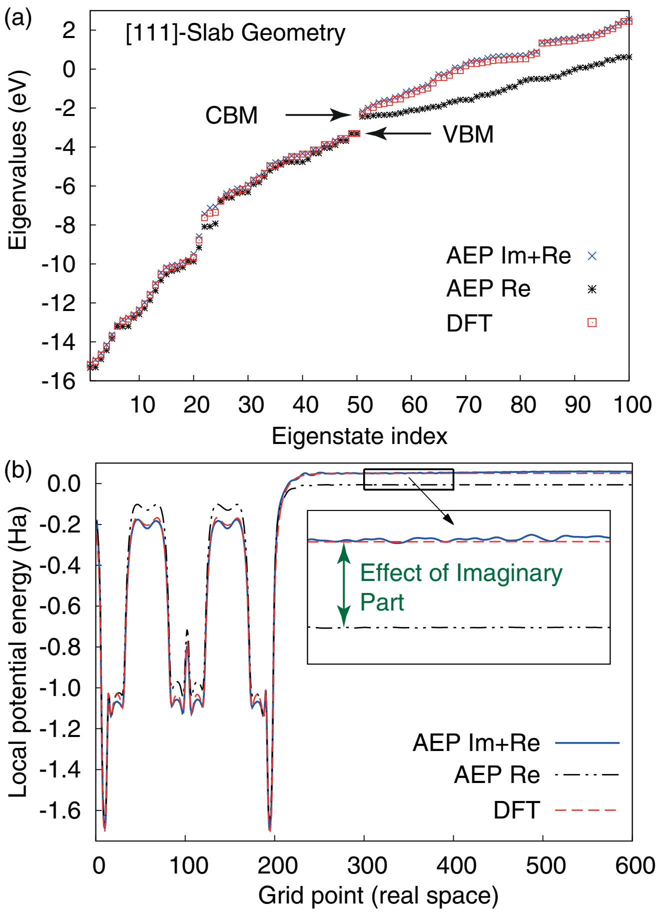

FIG. 4. (a) Eigenvalues aligned at the VBM obtained for a slab [111] geometry (24 Si and four H atoms) using AEPs including the imaginary and the real components of the pseudopotential (blue crosses), including only the real component (black star) and obtained from DFT (red squares). (b) Local potentials obtained for AEPs using real and imaginary parts (solid blue line), using the real part only (dot-dashed black line), and DFT potential (dashed red line).

the imaginary component we make a similar approximation $\mathrm{Im}\, v_{\mathrm{H1,2}}(G) = \mathrm{Im}\, v_{\mathrm{H1,2}}(|G|)$, keeping in mind that $\mathrm{Im}\, v_{\mathrm{H1,2}}(G) = -\mathrm{Im}\, v_{\mathrm{H1,2}}(-G)$. When we extract the passivant AEPs from Eq. (7) using a slab geometry Fig. 1(a) we obtain AEPs for two passivants. If these passivants are identical (in case of a passivants for a group IV semiconductor such as C, Si, or Ge), then their real parts are identical and their imaginary parts have same magnitudes but opposite signs. This follows our expectation that the asymmetry in real space must be reversed at both interfaces. The real and imaginary parts of the passivant AEP are illustrated in Fig. 1(b) showing an even real and odd imaginary potential. We store our passivant AEP with the imaginary sign corresponding to the passivant orientation [111] in the slab geometry (pointing upwards).

The contribution of the passivants in Eq. (6) to the total $\boldsymbol{G}$-space potential is written as

$$\begin{aligned} V_{\mathrm{H}}(\boldsymbol{G}) &= \frac{1}{\Omega_c}\sum_n^{N_H} \mathrm{e}^{-i\boldsymbol{G}\cdot\boldsymbol{\tau}_{Hn}} v_{\mathrm{H}}(\boldsymbol{G}) \\ &\approx \frac{1}{\Omega_c}\sum_n^{N_H} \mathrm{e}^{-i\boldsymbol{G}\cdot\boldsymbol{\tau}_{Hn}} \left(\mathrm{Re}\, v_{\mathrm{H}}(G) + i\frac{\boldsymbol{G}\cdot\boldsymbol{R}_p}{|\boldsymbol{G}||\boldsymbol{R}_p|}\,\mathrm{Im}\, v_{\mathrm{H}}(G)\right), \end{aligned} \tag{9}$$

where $\boldsymbol{R}_p$ is the real-space surface normal vector in Cartesian coordinates, denoting the direction of the antisymmetric component introduced by the imaginary part. Equation (9) represents a generalization of the one dimensional case where $\boldsymbol{G}$ and $\boldsymbol{R}_p$ are parallel or antiparallel to a situation where they have arbitrary orientation. The only known solutions are for the limiting cases of parallel/antiparallel vectors (prefactor to imaginary part $1/-1$) or perpendicular (prefactor to imaginary part 0 as we want spherical (real) potentials in the plane). We use a cosine function (dot product) connecting both cases as the simplest possible assumption. Figure 1(c) shows the qualitative situation with the AEP in real space originating from the real and imaginary components of the $\boldsymbol{G}$-space passivant AEP. As will be demonstrated further, it is advantageous to apply a weight factor w to the imaginary part in certain circumstances:

$$\begin{aligned} V_{\mathrm{H}}(\boldsymbol{G}) = \frac{1}{\Omega_c}\sum_n^{N_H} \mathrm{e}^{-i\boldsymbol{G}\cdot\boldsymbol{\tau}_{Hn}} \Bigg(&\mathrm{Re}\, v_{\mathrm{H}}(G) \\ &+ i\frac{\boldsymbol{G}\cdot\boldsymbol{R}_p}{|\boldsymbol{G}||\boldsymbol{R}_p|}\, w\, \mathrm{Im}\, v_{\mathrm{H}}(G)\Bigg). \end{aligned} \tag{10}$$

III. CALCULATION OF AEPS FOR SILICON PASSIVANTS

The methodology section describes the procedure in a general way. In practice, two different semiconductor slab

TABLE I. Structural parameters and band gap at the $\overline{\Gamma}$ point for Si slabs with zinc-blende structure and with different crystallographic orientations. The hydrogen density on the surface is given as $\rho(\mathrm{H})$ and the minimum distance between passivant hydrogens as R_{min}.

slab direction	[100]	[110]	[111]
N_{Si}	16	28	24
N_H	4	4	4
$\rho(H)(1/\mathrm{nm}^2)$	13.4	9.4	7.7
R_{min} (H-H) (Å)	1.51	3.12	3.87
E_{gap} (DFT) (eV)	0.896	0.906	1.004
E_{gap} (AEP) (eV)	0.987	1.019	1.133

geometries are used, denoted as slab A and slab B in the previous section, and shown in Fig. 2(a). The slabs are oriented along the [111] crystallographic direction and the bonds to the passivant atoms point in this direction as well, i.e., normal to the surface. We use elongated supercells of around 11.4 nm length in order to obtain a dense grid of G points. The DFT calculations are performed with the code ABINIT [32], using an energy cutoff of 35 Hartree and a k-point mesh of $12\times12\times1$ points. The Si-H bond are structurally relaxed in the [111] direction. We use Troullier-Martins norm-conserving pseudopotentials for the DFT calculation and for the nonlocal part of the pseudopotential in the AEP method [7]. The hydrogen atoms for the III-V and the II-VI materials are pseudohydrogens with fractional charges as typically used in DFT calculations [33,34], which correspond to an "ideal" passivation. One should keep in mind that some experimental situations will differ from this artificial case. The approach suggested, however, does not rely on the use of pseudohydrogens with fractional charge, but allows to introduce any atomic passivant.

The results for the passivant (hydrogen) AEP of silicon is shown in Fig. 2(b). The real part is shown in black, while the imaginary part of the potential is shown in red. The symbols show the discrete data points we obtain directly from the processing of the DFT calculations. The straight lines are cubic spline interpolations through the data points. In the region of $|\boldsymbol{G}| = n\,2\pi\sqrt{3}/(a_0)$ (for silicon $|\boldsymbol{G}| = n\,1.042$ in units of 1/a.u.), where n is an integer and a_0 the bulk lattice constant, the data point extraction suffers from the error which is intrinsically carried over from our bulk AEPs, i.e., the AEPs for silicon in this case. Since the goal for our passivant AEP is not to correct the deviations existing within the bulk AEPs, we omit the data points in the vicinity of these $|\boldsymbol{G}|$ values. By using these data points, one may indeed obtain better agreement than by ignoring them for the specific structure, but the transferability to structures with different dimensionality (see later) would be less accurate. The passivant effective potential shows a very steep imaginary part for small G values and a rather smooth real part, comparable to bulk AEPs [6].

IV. QUALITATIVE EFFECTS INTRODUCED BY THE IMAGINARY PART OF THE PASSIVANT AEP

Before assessing the quality of the derived pseudopotential by comparing eigenvalues and eigenfunctions with DFT, we consider a single passivant in an empty supercell. To estimate the effect of the newly defined imaginary component of the potential qualitatively, we plot in Fig. 3 the AEP for an isolated passivant in real space, orientated via the vector $\boldsymbol{R}_p$ [see Eq. (9)]. Only the imaginary part of the $\boldsymbol{G}$-space potential is shown. The corresponding spherical real part is significantly deeper and spherical and not shown explicitly. The asymmetric part exhibits two components: the short-ranged component localized in the proximity of the core of the passivant and a long-ranged component that introduce a clear band-offset type potential. It is understandable that the surface dipole, which is a consequence of charge transfer around the passivant, will

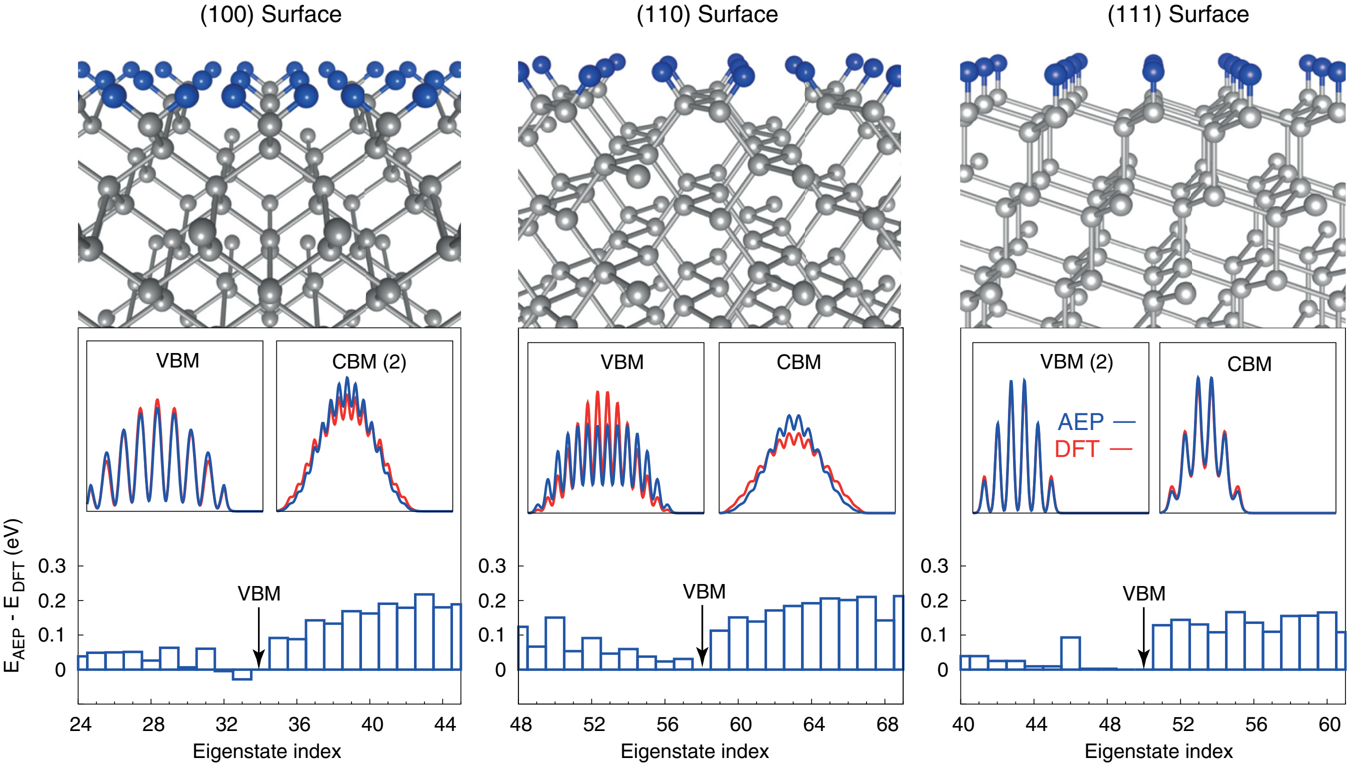

FIG. 5. Comparison between AEPs and DFT results for (100), (110), and (111) surfaces. The geometries of the different slabs are given at the top of the figure. The middle panels show the DFT (red) and AEP (blue) wave functions across the slabs along the growth direction. The degeneracy of the states is given in brackets. The lower part shows the difference between the AEP and the DFT eigenvalues as bar charts. The eigenvalues were aligned with respect to the VBM.

TABLE II. Structural parameters and band gaps of different nanowires. The Si and InP NWs have zinc-blende crystal structure, while the CdSe NW has wurtzite structure. N_{NW} represent number of atoms in the NWs. For InP [CdSe], the atom numbers are given as (number of In atoms, number of P atoms) [(number of Cd atoms, number of Se atoms)]. For InP, the number of passivants are given as (In-passivant, P-passivant), for CdSe as (Cd-passivant, Se-passivant). The hydrogen densities on the surfaces are given as $\rho(\mathrm{H})$ and the minimum distances between passivant hydrogens as R_{min}.

NW	Si				InP			CdSe
Diameter (nm)	1.3	2.1	3.0	4.5	1.3	1.7	1.6	1.4
N_{NW}	37	97	185	437	(16,21)	(32,25)	(26,26)	(24,24)
N_{H}	28	44	60	92	(4,24)	(32,4)	(16,16)	(18,18)
$\rho(\mathrm{H})$ $(1/\mathrm{nm}^2)$	12.47	12.37	12.33	11.99	11.50	11.14	10.76	11.69
R_{min} (H-H) (Å)	1.73	1.63	1.60	1.77	2.40	2.24	2.08	1.31
E_{gap} (DFT) (eV)	2.147	1.401	1.156	0.878	1.771	1.095	1.207	1.475
E_{gap} (AEP) (eV)	2.165	1.472	1.233	0.965	1.911	1.082	1.273	1.628

lead to such a band offset. It is reassuring to observe that the imaginary part of the potential is able to capture this effect.

V. ASSESSMENT OF THE QUALITY OF THE AEP FOR DIFFERENT SURFACES

The slab [111] structure [Fig. 2(a)], which represents the passivation of a (111) surface, is the geometry used to generate the AEP. As a first step, we compare the DFT results with the AEP results for a similar, although slightly longer (24 Si atoms and four hydrogens) structure. This calculation represents the simplest test since transferability is only marginally challenged (slightly longer slab) by this comparison. In Fig. 4(a), we plot the eigenvalues of the long [111] slab calculated via DFT (red), AEP only taking the real part into account (black) and the full AEP with real and imaginary components (blue). The band gap is located around state index 50. It is obvious that the imaginary part of the potential improves the quality of the states above band gap significantly. This is a direct consequence of the introduced band-offset discussed previously. In Fig. 4(b), we plot the local potential in real space of the entire slab along the [111] direction, again comparing DFT with real-only-AEP and full-AEP. We see that only the full-AEP result agrees well with the DFT results for the vacuum level.

Next, we want to challenge the transferability of the derived AEPs by comparing different slab orientations. In Table I, we summarize some relevant structural information. In Fig. 5, we plot the atomic structures of the different surfaces, the valence-band maximum (VBM) an the conduction-band minimum (CBM) wave functions calculated with DFT (red) and with AEPs (blue) along with error bars for the eigenvalue differences for states around the band gap, aligned at the VBM level. Our errors are within a range of 0.2 eV and occur mainly for the conduction-band states. Here we have to stress that the error of the AEP for the bulk band gap of Si is 87 meV [6]. So all the conduction-band states suffer from the 87 meV error coming from the bulk Si AEP and of the errors introduced by the passivant AEP. Both errors seem to be of similar magnitude, which substantiates the good quality of our approach.

VI. RESULTS FOR Si, InP AND CdSe NANOWIRES

The areas of application of our AEPs are nanostructures and we therefore first assess the quality of our results for nanowires. The structural information is given in Table II and a graphical representation of the atomic positions are given in Fig. 6(a) for a Si nanowire with 3 nm diameter. Each nanowire is constructed along the [100] direction for Si and InP and along the [0001] direction the wurtzite CdSe structure. The surfaces of the nanowires are terminated in such a way that each atom has only one or two passivants.

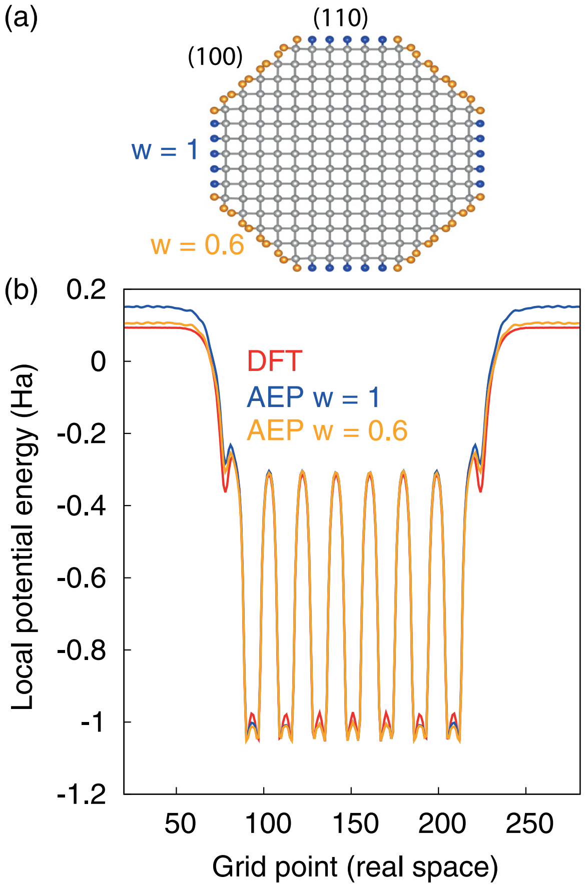

FIG. 6. (a) The geometry of the Si nanowire with a diameter of 3 nm. The hydrogens carrying a weight parameter [w in Eq. (10)] of $w = 0.6$ are shown as orange spheres, while the unweighted hydrogens ($w = 1$) are shown in blue. (b) Corresponding local potential.

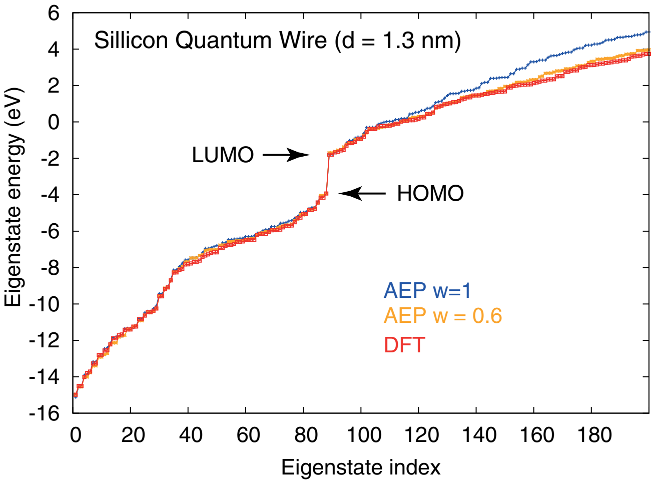

FIG. 7. First two hundred eigenvalues of the Si NW with 1.3 nm diameter (see Table II for structural details). The introduction of the weight factors (orange symbols) is shown to improve the quality of the previous results (blue symbols) for states excited more than 2 eV above the band gap. Red and orange symbols overlap nearly in the entire region.

TABLE III. Structural parameters and band gaps of different Si quantum dots. N_{Si} gives the number of Si atoms in the quantum dot and N_{H} the number of hydrogen passivants. The hydrogen densities on the surfaces are given as $\rho(\mathrm{H})$ and the minimum distances between passivant hydrogens as R_{min}.

Diameter (nm)	1.4	2.2	2.5	3.0
N_{Si}	87	281	465	705
N_{H}	76	172	228	300
$\rho(\mathrm{H})$ $(1/\mathrm{nm}^2)$	12.49	11.54	11.21	10.56
R_{min} (H-H) (Å)	2.48	2.01	1.82	2.01
E_{gap} (DFT) (eV)	2.692	1.877	1.664	1.498
E_{gap} (AEP) (eV)	2.723	1.944	1.755	1.536

The real-space potential is given in Fig. 6(b) in a similar way it was shown for the [111] slab in Fig. 4. The comparison between DFT (red) and AEP (blue) shows that the AEP reproduces the potential very well in general but significantly overestimates the band offset (the blue line in the vacuum region is significantly above the red line). This effect is related to the density of hydrogen atoms on the surface. As seen from Table II the hydrogen atom surface density is around 12 H-atoms/nm^2 in Si NWs, while it is 7.7 H atoms/nm^2 in the [111] Si slab (Table I) used in the AEP construction. Hence, we look for a way to systematically reduce the generated offset based on a density argument. A closer look at the NW geometry, shown in Fig. 6(a), reveals that it is composed of facets belonging to {100} and {110} planes. From Table I, we observe that the H density is quite different on both surfaces (13.4 H atoms/nm^2 and 9.4 H atoms/nm^2, respectively). For the high-density {100} surfaces, two hydrogen atoms are connected to one Si atom. We use this characteristic to apply weights: if a surface Si atom is passivated by two hydrogen atoms, then the density is high and we apply a weight in Eq. (10) of 0.6, which corresponds to the ratio of the densities between slab [111] and [100]. In Fig. 6(a), we marked the hydrogen atoms carrying a weight as orange spheres and see that they are mostly localized on the {100} planes. The results for the potential in the vacuum region, i.e., the offset, is significantly improved by the use of weights, as can be seen (orange curve) in Fig. 6(b).

We tested a more sophisticated approach, where we derived two passivant AEPs, one generated from a [111] slab calculation and one from a [100] slab calculation. We used both potentials on the respective facets of a silicon NW with 3.0 nm diameter [as shown in Fig. 6(a)]. The results were improved for states close to the band gap from an error of 30 meV to below 10 meV. However, this improvement on already very small errors, was not systematic for all the states considered (not shown). We conclude that an improvement of the results is possible using this technique, which has the benefit to contain no weight parameter. However, for our present purpose, the results of the weighted passivants have more than satisfactory quality and bare the advantage to lead to a simpler method [need for only one passivant AEP per (pseudo)hydrogen]. The

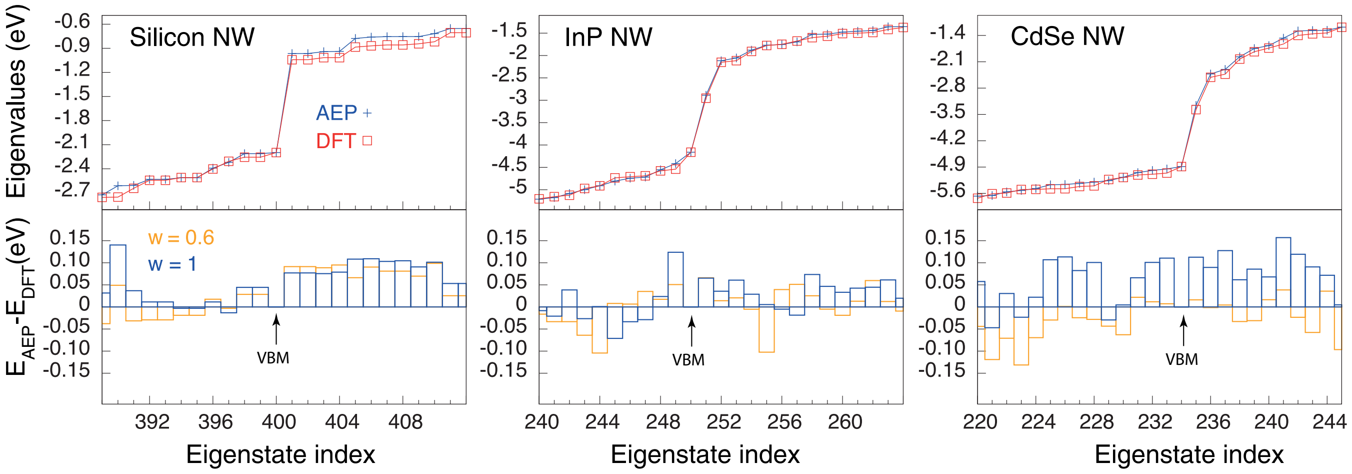

FIG. 8. Top panels: Eigenvalues for Si, InP, and CdSe nanowires in the proximity of the band gap. Lower panels: Bar charts showing the differences between DFT results and the AEP result including the weight strategy (orange) and the AEP result without weight (blue).

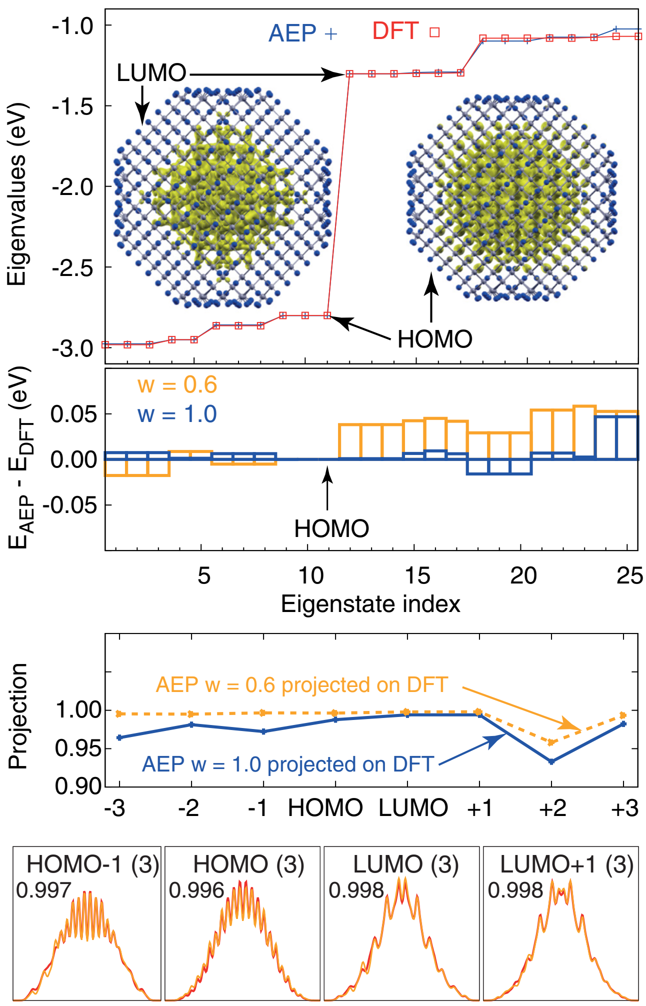

FIG. 9. DFT and AEP results for a silicon quantum dot with 3.0 nm diameter (see Table III). The eigenvalues and the eigenvalue differences are given in the upper two panels. The projection is calculated as $\langle \psi^{\mathrm{AEP}} \mid \psi^{\mathrm{DFT}} \rangle$ and describes the quality of the wave functions. Selected wave functions are given explicitly in one-dimension across the quantum dot in the lower panels. The insets of the upper panel show three-dimensional plots of the isosurfaces of the HOMO and LUMO wave functions.

results for the potential in the vacuum region, i.e., the offset, is significantly improved by the use of weights, as can be seen (orange curve) in Fig. 6(b).

The main benefit of introducing a weight to the imaginary part is to correct the offset, as just shown, which has direct repercussions on the eigenvalues of excited states close to the vacuum. In Fig. 7, which shows the eigenvalues in a large energy range, starting at the lowest energy eigenstate at −15 eV up to 6 eV above the gap. The calculations without weight (blue data points) are in good agreement with the DFT results (red data points) until an energy value of around 2 eV above the CBM. At higher energies deviations become significant, which are well corrected by the weighted potentials (orange data points).

Finally, we perform a quantitative comparison of the eigenvalues obtained for nanowires of different materials in Fig. 8. In the upper panels, we show a large energy range in the vicinity of the band gap. For all three materials, Si, InP, and CdSe the AEP results (blue crosses) are in very good agreement with the DFT results (red squares). The errors between the DFT and the AEP results are given as bar chart in the lower part of the figure, showing that all errors are below 150 meV, which is more than satisfactory. The introduction of the weight factor does not change the results significantly in this energy range, as is shown by the orange error bars in the lower panels of Fig. 8.

VII. RESULTS FOR Si QUANTUM DOTS

The final comparison for QDs is also the most challenging in terms of transferability as the passivant atoms point virtually in all directions. The structural information as well as the numerical results for the band gaps are given in Table III for four different silicon quantum dots. The average hydrogen density, as well as the minimum hydrogen separation R_{min}, are similar to the values we obtained for the nanowires (Table II). The band gaps are in good agreement to the DFT results for all the sizes considered. Next, we focus on our largest quantum dot with 3.0 nm diameter, which already represents are size comparable to experiment, and present a thorough analysis in Fig. 9.

In Fig. 9, we show the eigenvalues in a large range of energy as well as the error bars in the usual way. The quality of the results is excellent with errors below 50 meV. The quality of the wave function can be judged by projecting them onto the DFT wave functions: $\langle \psi^{\mathrm{AEP}} \mid \psi^{\mathrm{DFT}} \rangle$. We obtain values very close to 1.0, with some improvement through the use of the weight parameter [Eq. (10)]. In the lower part of Fig. 9, we show selected wave function as one dimensional

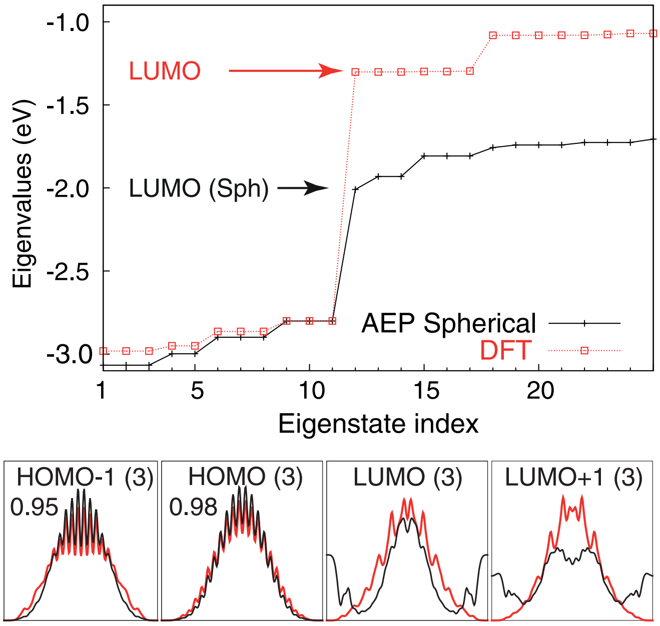

FIG. 10. (Top) Eigenvalues of the silicon quantum dot with 3.0 nm diameter calculated via DFT and calculated using AEPs without the imaginary component (AEP spherical). (Bottom) Selected wave functions around the band gap calculated with DFT and spherical AEPs.

plots across the center of the quantum dot as illustration. Wave functions of degenerate eigenstates are summed and their degeneracy is denoted in brackets. The values close to one are the numerical values of the projection onto the DFT wave functions. The DFT results (red) and the AEP results with weight (orange) show very good agreement. The insets in the upper part of the figure show three dimensional isosurface plots of the highest occupied nanostructure state (HOMO) and the lowest unoccupied nanostructure state (LUMO) showing clearly confined and well behaved envelope S-type states.

Finally, we reassess the importance of the imaginary part (which is responsible for the asphericity of the potential) by calculating the eigenvalues and eigenstates using only the real-part of the AEP. The results of this "spherical approximation" is shown in Fig. 10. We notice very large qualitative discrepancies in the LUMO states and some quantitive differences in the HOMO states. The surface dipoles—which can be modeled by our nonspherical complex passivant AEP—and the resulting band-offset to vacuum are essential for the LUMO states of Si quantum dots. The degeneracy of the LUMO is entirely different when the imaginary part of the potential is neglected. The splitting between the HOMO states tends to be overestimated in the spherical passivant approximation.

VIII. CONCLUSION

In conclusion, we propose a new method to derive passivant AEPs that carry an imaginary part in their G-space representation, which translates into a nonspherical and noninversion symmetric real-space potential. The nonsphericity of the AEPs is shown to improve the results compared to the more traditional spherical pseudopotentials at no additional computational cost.

However, these new type of pseudopotentials require the definition of a surface normal to the nanostructure which is required for the orientation of the passivant potential. We show that the imaginary part introduces a local asymmetry in the vicinity of the passivant atom (which is rather small compared to the symmetric part) as well as a band offset between vacuum and nanostructure. This band offset effect is in nice agreement with our general understanding of surface induced dipoles developing at surfaces and inducing a band offset. We obtain an excellent transferability of the passivant AEPs concerning the local asymmetry effect, but a less transferable band offset contribution. To improve on this latter point, we introduced a weight parameter that corrects the band offset, which is important for highly excited states. We link this correction to the passivant density and derive a simple method to apply it. With this approach, we seem to be able to capture the self-consistent charge rearrangement effect leading to surface dipoles.

For the test cases of silicon, InP and CdSe nanostructures we obtain for the smaller structures (where surface effects are very important) eigenvalues within 200 meV of the *ab initio* DFT result, which represents a significant improvement over former approaches that only lead to a qualitative result for the passivant, such as an absence of surface states within the band bap. For larger QD structures, our agreement with DFT improves to well below 100 meV error. Our method is rather universal, so that not only passivant such as hydrogen or pseudohydrogen (for group III-V and II-VI as done here) can be considered, but more realistic surfaces as well. The main benefits of the approach is twofold. First, it opens the possibility to study surface related phenomena at the AEP level, i.e., involving up to one hundred thousand atoms [7]. For colloidal QDs, the influence of the surface termination/passivation on their electronic and optical properties is known to be large and need to be taken into account for the elaboration of a predictive theory. Second, it represents a large simplification in the generation of the pseudopotentials, since we elaborate a simple analytic connection between the DFT Kohn-Sham potential and the passivant AEP.

ACKNOWLEDGMENTS

We thank Daniel Mourad, Frank Zirkelbach, and Jerome Jackson for stimulating discussions. Most of the large-scale DFT calculations were preformed on the Cray XC40 Hazel Hen Supercomputer Cluster at the High Performance Computing Center Stuttgart (HLRS). D.A. acknowledges financial support by the Deutsche Forschungsgemeinschaft through the Sonderforschungsbereich 716.

---

[1] M. S. Nikolic, M. Krack, V. Aleksandrovic, A. Kornowski, S. Förster, and H. Weller, Angew. Chem. Int. Edit. **45**, 6577 (2006).
[2] V. I. Klimov, S. A. Ivanov, J. Nanda, M. Achermann, I. Bezel, J. A. McGuire, and A. Piryatinski, Nature (London) **447**, 441 (2007).
[3] Z. Hens and J. C. Martins, Chem. Mater. **25**, 1211 (2013).
[4] P. D. Howes, R. Chandrawati, and M. M. Stevens, Science **346**, 1247390 (2014).
[5] M. V. Kovalenko, L. Manna, A. Cabot, Z. Hens, D. V. Talapin, C. R. Kagan, V. I. Klimov, A. L. Rogach, P. Reiss, D. J. Milliron *et al.*, ACS Nano **9**, 1012 (2015).
[6] J. R. Cárdenas and G. Bester, Phys. Rev. B **86**, 115332 (2012).
[7] F. Zirkelbach, P. Y. Prodhomme, P. Han, R. Cherian, and G. Bester, Phys. Rev. B **91**, 075119 (2015).
[8] L.-W. Wang and A. Zunger, Phys. Rev. B **51**, 17398 (1995).
[9] H. Fu and A. Zunger, Phys. Rev. B **55**, 1642 (1997).
[10] A. Franceschetti and A. Zunger, Phys. Rev. Lett. **78**, 915 (1997).
[11] L.-W. Wang, A. Franceschetti, and A. Zunger, Phys. Rev. Lett. **78**, 2819 (1997).
[12] F. A. Reboredo and A. Zunger, Phys. Rev. B **63**, 235314 (2001).
[13] L.-W. Wang, M. Califano, A. Zunger, and A. Franceschetti, Phys. Rev. Lett. **91**, 056404 (2003).
[14] G. Bester, S. Nair, and A. Zunger, Phys. Rev. B **67**, 161306(R) (2003).
[15] G. Bester, J. Phys.: Condens. Matter **21**, 023202 (2009).
[16] L.-W. Wang and A. Zunger, Phys. Rev. B **53**, 9579 (1996).
[17] P. A. Graf, K. Kim, W. B. Jones, and L.-W. Wang, J. Comp. Phys. **224**, 824 (2007).
[18] M. Califano, G. Bester, and A. Zunger, Nano Lett. **3**, 1197 (2003).

[19] C. Sevik and C. Bulutay, Phys. Rev. B **77**, 125414 (2008).
[20] S. Baskoutas and G. Bester, J. Phys. Chem. C **115**, 15862 (2011).
[21] L.-W. Wang and A. Zunger, J. Phys. Chem. **98**, 2158 (1994).
[22] J. T. Hu, L. S. Li, W. D. Yang, L. Manna, L.-W. Wang, and A. P. Alivisatos, Science **292**, 2060 (2001).
[23] M. Califano and A. Zunger, Phys. Rev. B **70**, 165317 (2004).
[24] P. Hohenberg and W. Kohn, Phys. Rev. **136**, B864 (1964).
[25] W. Kohn and L. J. Sham, Phys. Rev. **140**, A1133 (1965).
[26] U. von Barth and C. D. Gelatt, Phys. Rev. B **21**, 2222 (1980).
[27] L. Kleinman and D. M. Bylander, Phys. Rev. Lett. **48**, 1425 (1982).
[28] N. Troullier and J. L. Martins, Phys. Rev. B **43**, 1993 (1991).
[29] O. K. Andersen, *Computational Methods in Band Theory* (Plenum Press, New York, 1971).
[30] O. K. Andersen, Phys. Rev. B **12**, 3060 (1975).
[31] R. M. Martin, *Electronic Structure: Basic Theory and Practical Methods* (Cambridge University Press, Cambridge, UK, 2004).
[32] X. Gonze, B. Amadon, P. M. Anglade, J. M. Beuken, F. Bottin, P. Boulanger, F. Bruneval, D. Caliste, M. Côté, T. Deutsch *et al.*, Comput. Phys. Commun. **180**, 2582 (2009).
[33] A. Molina-Sánchez, A. García-Cristóbal, and G. Bester, Phys. Rev. B **86**, 205430 (2012).
[34] X. Huang, E. Lindgren, and J. R. Chelikowsky, Phys. Rev. B **71**, 165328 (2005).